AIAA JOURNAL
Vol. 31, No. 2, February 1993

Application of Scalar Implicit Approximate Factorization for Underwater Magnetohydrodynamic Propulsion Concept Analyses

D. Choi* and C. J. Knight†
Textron Defense Systems, Everett, Massachusetts 02149

Numerical procedures have been developed to analyze multidimensional flow and imposed electromagnetic fields associated with a marine magnetohydrodynamic (MHD) propulsion concept. Chorin's artificial compressibility treatment is applied to determine the incompressible flowfield both internal and external to the MHD thruster, using a zonal formulation. Both inviscid and viscous flow are considered. Determination of three-dimensional magnetic, electric, and Lorentz force fields is based on suitable idealizations. This provides indicative results without getting into detailed system design considerations. Among other conclusions, it is established that secondary flow induced by the nonuniform Lorentz force is not a key issue in the magnet end-turn regions.

Introduction

A MAGNETOHYDRODYNAMIC propulsion system could be a very attractive alternative for marine vehicles due to its mechanical simplicity and other factors. The underlying principle is that electrical current flow in the presence of a transverse magnet field will produce a body force on the conducting medium, such as seawater.[1] Thus, there are no external moving parts. Reasonable magnetohydrodynamic (MHD) propulsion efficiencies appear feasible with proper design. That typically involves low current density (<500 A/m^2), large thruster volume, and small velocity increment. This implies that MHD propulsion is most appropriately applied to a large vessel, such as a submarine. Onboard electrical power generation would replace the propeller drive system.

A variety of designs can be considered for a nuclear-powered submarine with an MHD propulsion system. Two basic geometrical configurations, shown in Fig. 1, are consistent with maintaining integrity of the pressure shell. The first conforms to the natural shape of the submarine (i.e., cylindrical) and involves an annular hull-mounted thruster. The second uses an add-on, almost stand-alone engine attached to the submarine, which is referred to as pod mounted. The hull-mounted configuration generally involves greater capture area, larger mass flow of seawater, and consequently greater thrust for given exit velocity. The pod-mounted configuration can also be unwieldy during dry-docking. These and other considerations favor the hull-mounted thruster for a retrofit system.

At least three MHD configurations can be put forward: linear, annular, and squirrel cage.[2] In terms of high propulsion efficiency and low magnetic field leakage, an annular arrangement is the most promising alternative. Away from the end-turn regions, near inlet and exit, this involves radial electrical current flow and an azimuthal magnetic field to produce axial thrust. Magnet end-turns would be enclosed within suitable hydrodynamically shaped struts, shown in Fig. 1 for the hull-mounted thruster. This paper is restricted to such a configuration. We address development of computational tools for analysis of both flow and electromagnetic fields.

An outline of the content is as follows. A zonal code for incompressible flow is first described. This uses an idealized model of the Lorentz force distribution, and a simultaneous solution is obtained for regions internal and external to the thruster. Two-dimensional results are given for both inviscid and viscous flow, the latter based on two-equation turbulence modeling. Numerical treatment of the three-dimensional electromagnetic fields is next addressed for an idealized configuration. Negligible magnetic Reynolds number is assumed, and effects of flow nonuniformity on the electric field are not considered. The Lorentz force distribution derived in this way is then employed in a three-dimensional inviscid simulation of flow in the entrance region of an MHD propulsion system. Conclusions are given at the end of the paper.

Numerical Method for Flowfield

For general application, a code must be capable of handling flow in curvilinear coordinates, treat multiply connected domains to simulate conditions both internal and external to the thruster, and incorporate MHD source terms due to Lorentz $J \times B$ forces. A zonal formulation is required. Fortunately, we had already developed a sophisticated three-dimensional viscous turbomachinery code with such features[3-5] that could be adapted to marine systems. An essential ingredient in doing this was an efficient means of treating incompressible flowfields.

Chorin's artificial compressibility method[6] was chosen after considering other alternatives (e.g., pressure-correction meth-

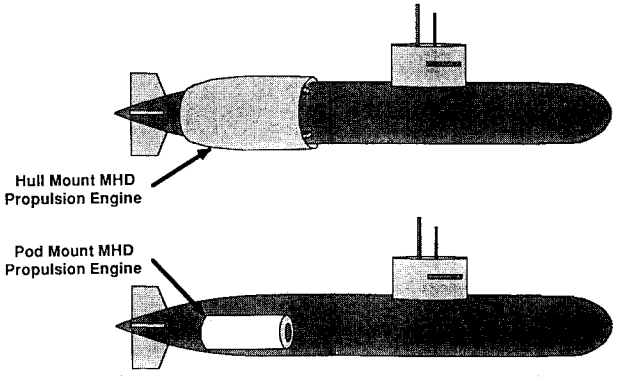

Fig. 1 Two submarine propulsion system mounting concepts.

Presented as Paper 91-0386 at the AIAA 29th Aerospace Sciences Meeting, Reno, NV, Jan. 7-10, 1991; received May 31, 1991; revision received March 30, 1992; accepted for publication March 30, 1992.

*Principal Research Scientist, 2385 Revere Beach Parkway.
†Program Director; currently at Jason Associates at Navy H/HTC, CARDEROCKDIV, NSWC, David Taylor Model Basin, Building 17E, Room 120, Bethesda, MD 20084.

ods). This approach involves modifying the continuity equation through addition of a pressure time-derivative term, which introduces a finite pseudowave speed. The basic ideas can be illustrated for two-dimensional inviscid flow in Cartesian coordinates, in which case

$$\frac{\partial Q}{\partial t}+\frac{\partial F}{\partial x}+\frac{\partial G}{\partial y}=H$$

$$Q^T=(p/\beta^2,\ u,\ v)$$

$$F^T=(u,\ u^2+p,\ uv) \tag{1}$$

$$G^T=(v,\ uv,\ v^2+p)$$

$$H^T=(0,\ f_x,\ f_y)$$

where f_x and f_y are the Lorentz body force components per unit mass, and p denotes pressure divided by density. Joule heating is small, so there is no need to consider an energy equation. Note that the converged steady-state solution will not be affected by the artificial term.

Choi and Merkle[7] investigated the stability and convergence characteristics of Chorin's method using a linear block implicit factorization scheme. They recommended the artificial compressibility factor in the continuity equation, β, be chosen near the freestream velocity to have the best convergence. The same conclusion was arrived at by Rizzi and Eriksson.[8]

Scalar implicit approximate factorization is used here. In differential form and Cartesian coordinates, this entails

$$\left(I+\delta t\Lambda_x\frac{\partial}{\partial x}\right)\cdot S_x\delta Q^*=S_x\Delta Q$$

$$\left(I+\delta t\Lambda_y\frac{\partial}{\partial y}\right)\cdot S_y\delta Q=S_y\delta Q^* \tag{2}$$

where δQ is the change in solution vector over time step δt, ΔQ is proportional to the steady terms in Eq. (1), I is the identity matrix, Λ is a diagonal matrix of eigenvalues, S is a matrix of left eigenvectors, and subscripts x or y denote the respective Cartesian directions.

Characteristic directions are substantially different than in ordinary compressible fluid mechanics because time derivative terms are altered in Eq. (1). For example,

$$\Lambda_x=\mathrm{diag}\left(u,\ u+\sqrt{\beta^2+u^2},\ u-\sqrt{\beta^2+u^2}\right) \tag{3}$$

Thus, although the form of Eq. (2) is familiar in the computational fluid dynamics (CFD) community, the actual transformations involved are changed. Adaptation of the existing scalar-implicit turbomachinery code was considerably facilitated by the analogy between sound speed in a compressible formulation and pseudowave speeds in Chorin's method. Similar treatments have been used by others[9,10] so further elaboration will not be given here.

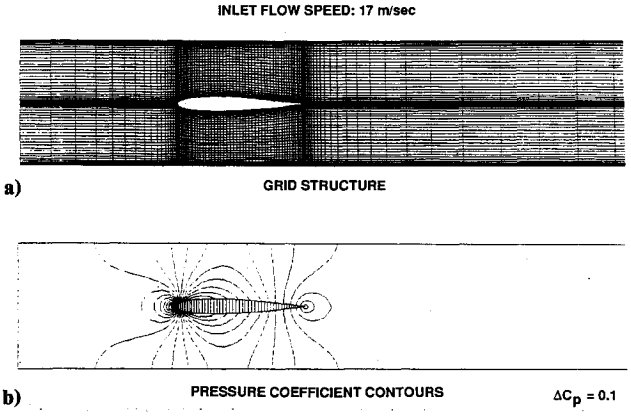

Fig. 2 Viscous incompressible flow around a NACA 0012 airfoil.

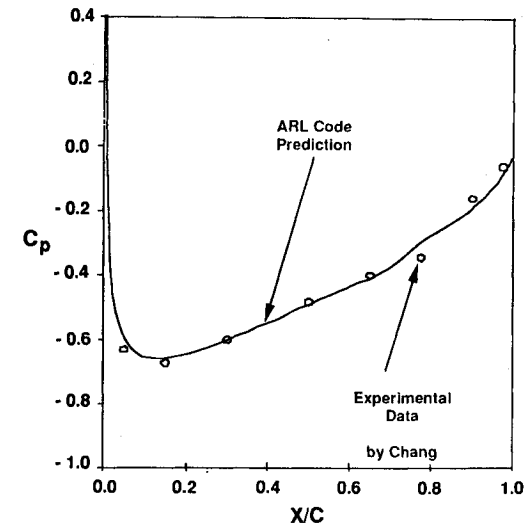

Fig. 3 Pressure coefficient profile on a NACA 0012 airfoil.

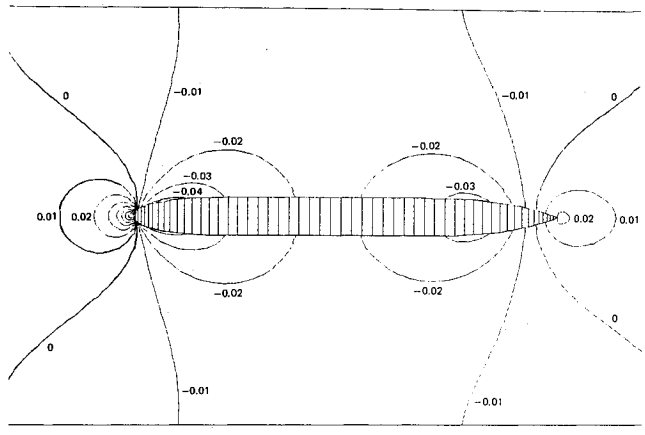

Fig. 4 Pressure coefficient contours around a submarine.

Coakley's q-ω turbulence model[11] was chosen because it is numerically compatible with asymptotic time integration procedures and because it has been extensively compared with relevant experimental data in our prior studies. Here $q=\sqrt{k}$ is a turbulent velocity scale and $\omega=\epsilon/k$ is an inverse eddy-decay time, where k is the turbulence kinetic energy and ϵ the isotropic dissipation rate. A wall-function treatment was implemented to reduce near-wall gridding requirements at high Reynolds number ($Re\sim 10^9$). This is based on using q in place of the friction velocity, $u^*=\sqrt{\tau_w/\rho}$, so that boundary-layer separation and reattachment are better handled.

A cell-based formulation is used to assure excellent conservation characteristics and achieve geometric flexibility. Boundary conditions are treated fully implicitly. This is essential to achieve a rate of convergence in fine-grid viscous regions comparable to that for inviscid regions. The procedure is considerably expedited by use of pseudocharacteristic relations. Fully implicit coupling is also maintained across zone interfaces through care in forming the coefficient matrix. Treatment of multiple zones is facilitated by use of pointer indices, duplicated storage near zone interfaces to avoid conditionals within DO loops, and efficient use of hardware gather-scatter operations.

The explicit calculation, or residual evaluation, uses second-order fully upwind differencing of inviscid terms based on pseudocharacteristics and second-order central differencing of

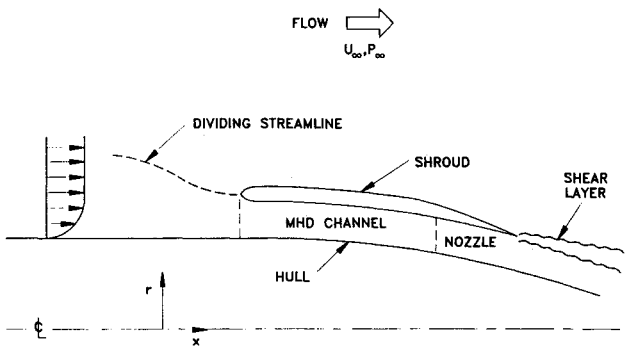

Fig. 5 Underwater MHD thruster modeling.

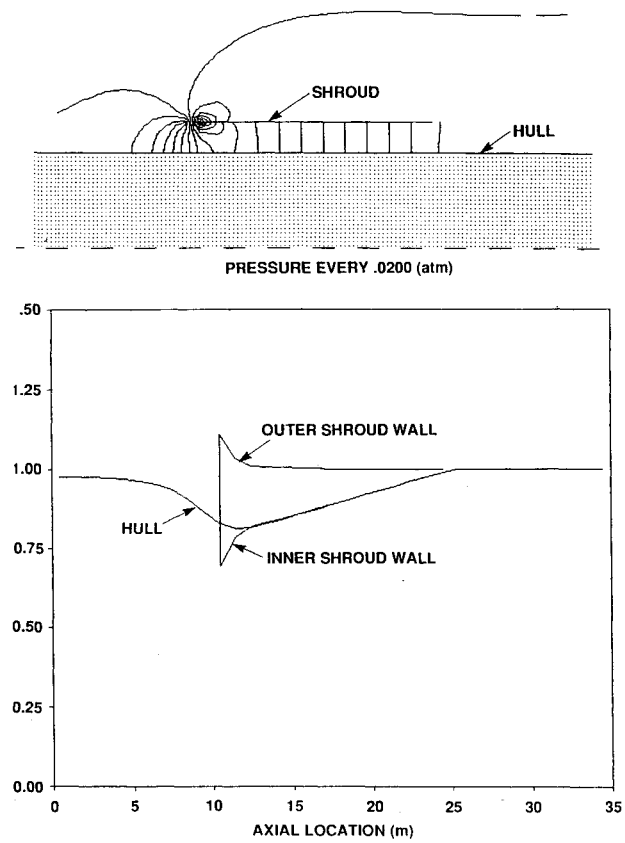

Fig. 6 Inviscid flow in an idealized MHD thruster.

viscous terms. For the implicit procedure, first-order upwinding is used and involves solving a series of scalar tridiagonal linear systems. This may affect convergence rate somewhat, but overall computational cost is relieved. The source terms from MHD Lorentz force and turbulence production/dissipation are treated by using a point implicit postprocessing update procedure.[3,5] Convergence is quite typically achieved in 200 time steps for an inviscid calculation and 500 steps for a viscous calculation, both for a "cold start" procedure. Computational performance for a three-dimensional code with six variables (p, V, q, ω) is equivalent to 10–15 μs per grid point per time step on a CRAY 2. About 30 CPU min would be required for a viscous simulation with 200,000 grid points on that machine. Our work was done on less powerful computers and, of course, takes longer.

Two-Dimensional Flow Results

A number of test cases were executed as part of the code development process. These will be summarized to demonstrate code capability. The discussion here is focused on the MHD two-dimensional code, which is available in both inviscid and viscous forms. In all cases, constant static pressure is imposed at the exit plane and the stagnation pressure profile is specified at the inflow plane. The coefficient of that profile is iteratively determined during the solution procedure based on the upstream running pseudocharacteristic, using a treatment analogous to that employed for compressible flow.[3]

The new incompressible flow solver has been applied to a flow around a NACA 0012 airfoil in a square duct (see Fig. 2). In Fig. 3, accuracy of the scheme was verified by comparing the computed pressure profile with experimental data obtained by Chang and Gessner.[12] This case was also considered with the compressible code at low Mach number, $M = 0.2$. The converged solutions obtained from the incompressible and low Mach number compressible equations are essentially identical. For this case, the turbulence model equations are integrated up to the wall by using a low Reynolds formulation of Coakley without wall function treatment.[11] That is quite feasible for $Re \sim 10^6$ and has been routinely done for turbomachinery.

The code was then adapted to axisymmetric geometries. A test case of particular interest involved a submarine configuration without appendages, as shown in Fig. 4. The hull geometry is derived from parametric relations given by Jackson[13] and includes an extended parallel midbody. Pressure coefficient contours are based on an inviscid simulation and should be representative of a high Reynolds number flowfield. Note that the pressure is reasonably uniform just upstream of the aft section where the MHD propulsion system may be located. This provides some basis for restricting attention to a smaller domain in subsequent calculations (primarily because they were done on a COMPAQ 386/25 PC). This is not essential in two dimensions but could be in three dimensions to limit the computational requirements.

A series of two-dimensional cases were then considered to assess flowfield issues for a local domain about the MHD thruster. The geometry and nomenclature is indicated in Fig. 5. Since the thruster is hull mounted, there will be a thick incoming boundary layer. A simple $1/r^2$ dependence was as-

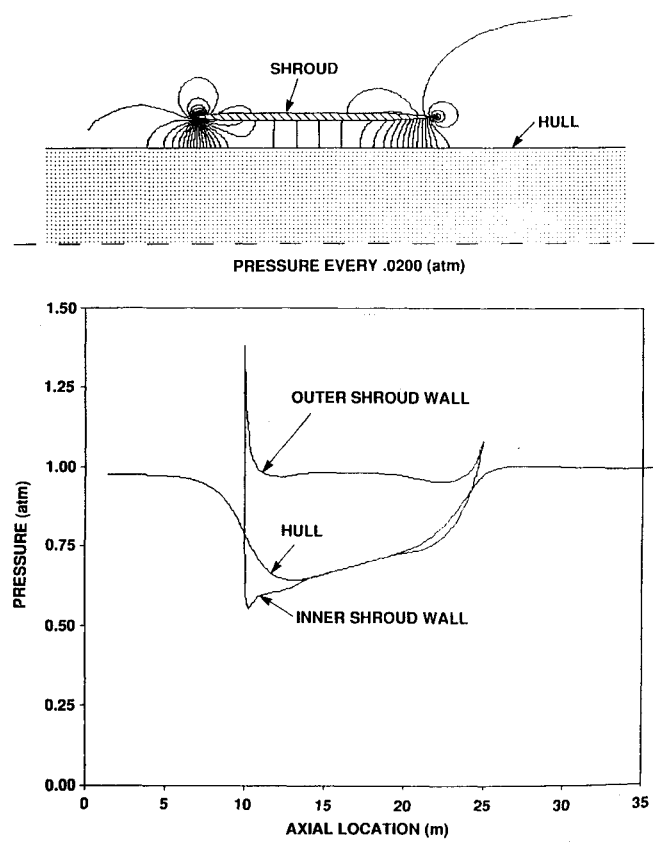

Fig. 7 Inviscid flow with a thick thruster shroud.

sumed for the Lorentz force density ($J \times B$) within the MHD channel, with no attempt to account for variation across boundary layers. The two-dimensional code also did not account for blockage by the magnet coil end-turns. Such ramifications can be pursued in later work.

First, we considered an inviscid case for an idealized MHD thruster with zero shroud thickness, as shown in Fig. 6. The local computation domain starts 10 m upstream of the MHD thruster, ends 10 m downstream of the thruster, and the length of the thruster is 15 m. An inflow hull boundary-layer profile was chosen based on a run length of 70 m. The freestream velocity is 10 m/s, and $J \times B$ is chosen to be 768.3 N/m^3 within the internal passage of the thruster. (That $J \times B$ corresponds to a large drag coefficient.) For this case, we used only 36 grid points in the axial direction and 40 grid points in the radial direction (20 in the thruster and 20 in the outer region). The thickness of the thruster shroud was assumed to be zero. As one can see in Fig. 6, the MHD effect lowers the pressure in the front portion of the thruster by accelerating flow into the thruster inlet, generates static pressure increase within the thruster at almost constant axial velocity, and achieves static pressure at the exit near its freestream value.

In Fig. 7, computational pressure results are shown for a thick thruster shroud case based on an $89 \times (20 + 20)$ grid. The shroud geometry is derived from the same sort of parametric relation as used for Fig. 4 but is adjusted to give 0.43 m thickness in the central region. The pressure peaks at the outer shroud wall indicate a need to improve the contouring of the shroud ends, perhaps with flaring, to prevent separation and possible drag increment induced by the pressure peak. This result indicates that the code can be used effectively for the design stage. Further work in this area is relevant. Figure 8 shows the effect of the hull contouring for inviscid flow. Note that variable area is now involved in the downstream portion of the MHD thruster. There are questions about the exit boundary treatment in this case, and the computational domain should be extended well aft of the stern. With constant hull radius, we verified there was no problem by considering successively larger domains.

Computational results for a viscous case are shown in Figs. 9 and 10. Figure 9 shows the $89 \times (42 + 32)$ grid system as well as pressure and radial velocity contours. Inlet freestream velocity is 10 m/s, and $J \times B$ is again 768.3 N/m^3, as for the inviscid cases. The Reynolds number based on the thruster length is 1.5×10^8. To highlight the flow-capturing process in front of the thruster inlet, only negative radial velocity contours are shown in the figure. In Fig. 10, axial velocity profiles are shown in six locations beginning 3.43 m upstream of the thruster and ending 1.65 m downstream. These profiles show how the flow develops in the inlet capture and the near-exhaust regions. For this case, Coakley's q-ω turbulence model equations were solved with a wall-function treatment. This avoids the need to deal with the sublayer region for a high Reynolds number flow.

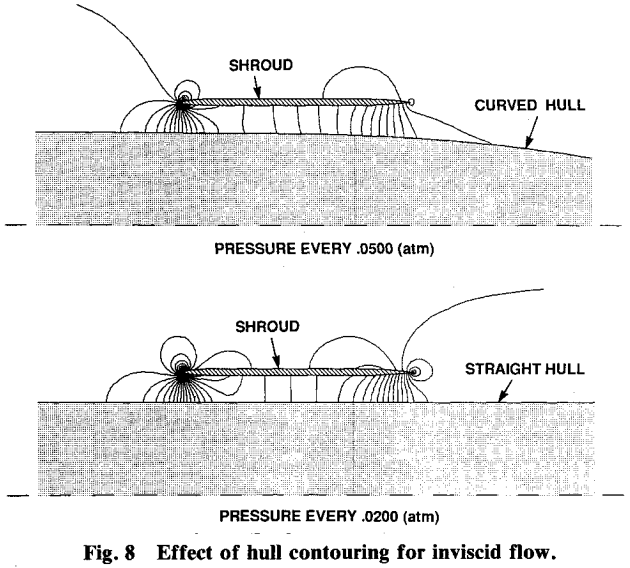

Fig. 8 Effect of hull contouring for inviscid flow.

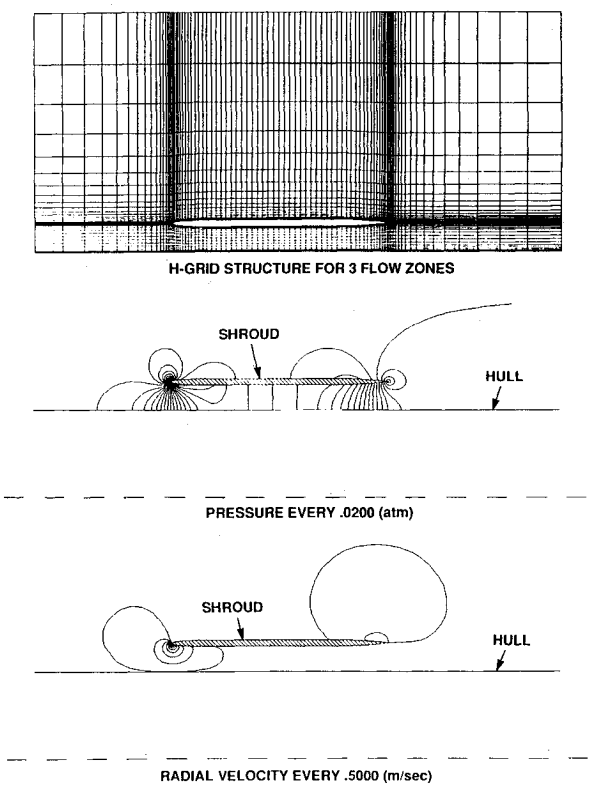

Fig. 9 Viscous flow using a 2-EQ turbulence model.

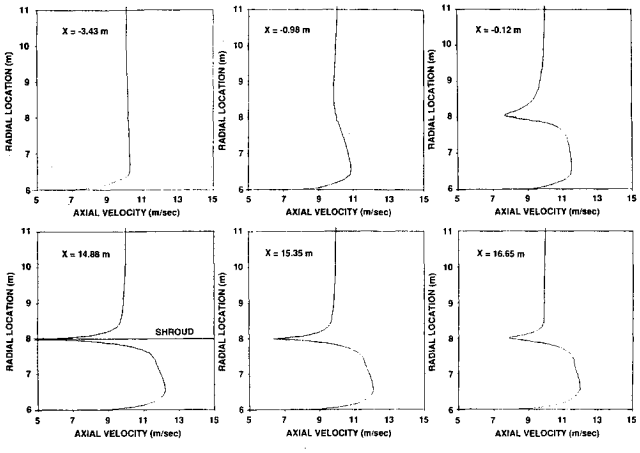

Fig. 10 Axial velocity profiles for straight-hull case.

Three-Dimensional Electromagnetic Fields

The results given in the preceding discussion are representative away from the end-turn regions. More complex phenomenology arises near the inlet and exit of the MHD thruster. Superconducting magnet coils turn across the flow channel as illustrated in Fig. 11. Thus, the predominantly azimuthal magnetic field within the MHD channel undergoes rapid transition, and the other two field components are activated. MHD electrodes also terminate so that electrical current is decreasing through the end-turn region in a fringing pattern. These factors imply a complex distribution of Lorentz force that may affect the flow capture process at the inlet as well as the exhaust stream. Flow is addressed later.

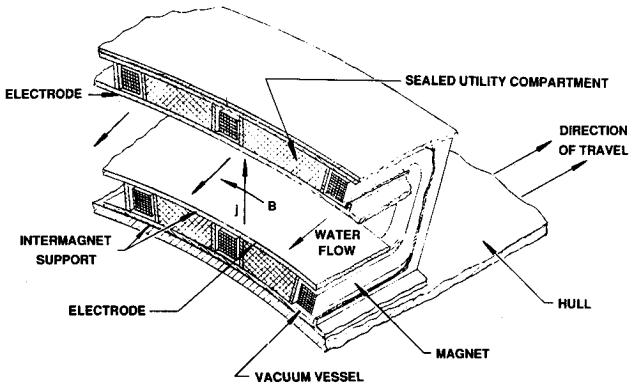

Fig. 11 Annular hull-mounted concept for magnetohydrodynamic submarine propulsion.

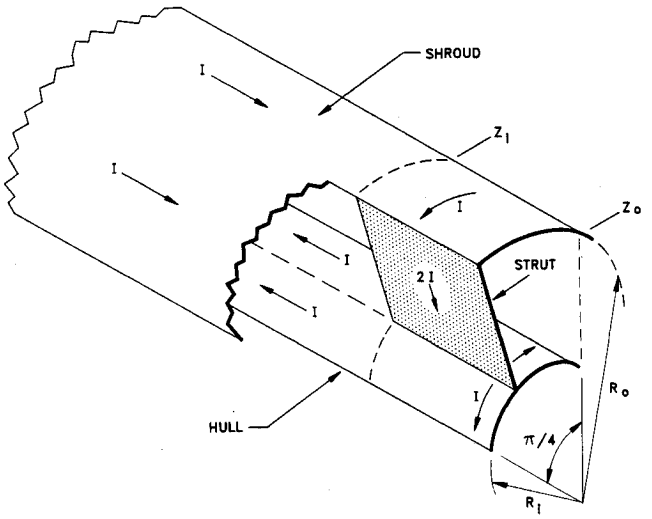

Fig. 12 One segment of an eight-post annular magnet configuration.

The discussion in this section focuses on numerically determining the electromagnetic fields for an idealized configuration. An actual design would most likely consist of magnet coils that are much thinner in the radial direction and much wider in the azimuthal direction. That minimizes azimuthal ripple in magnetic field within the channel as well as leakage into the external environment. Thin struts, to minimize flow blockage, can be achieved with a saddle coil configuration. Going to the extreme of infinitesimally thin coils is an obvious idealization.[14] This leads to a configuration consisting of two cylindrical shells joined by equispaced struts of finite axial length. We will be considering an eight-segment configuration so that each strut is placed $\pi/4$ rad apart. One segment of such an arrangement, involving a magnet coil pair, is shown in Fig. 12. Directions of surface current flow in the coils are also given, again involving an indicative idealization.

Further assumptions were made to render calculations more tractable. Within the context of the usual MHD approximations, Maxwell's equations reduce to

$$\begin{aligned} \text{curl}(\boldsymbol{E}) &= 0 \qquad \text{curl } \boldsymbol{B} = \mu \boldsymbol{J} \\ \text{div}(\boldsymbol{J}) &= 0 \qquad \text{div } \boldsymbol{B} = 0 \end{aligned} \tag{4}$$

where $\boldsymbol{E}$ is the electric field, $\boldsymbol{B}$ is the magnetic induction, and $\boldsymbol{J} = \sigma(\boldsymbol{E} + \boldsymbol{U} \times \boldsymbol{B})$ is the current density. For seawater, $\mu \sim 4\pi \times 10^{-7}$ H/m and $\sigma \sim 4$ mho/m. It will be adequate to set $\boldsymbol{J} = 0$ in determining $\boldsymbol{B}$ because the field due to the superconducting coils will totally dominate that due to current flow through the seawater. Thus, zero magnetic Reynolds number is assumed here. Introducing a vector potential such that $\boldsymbol{B} = \text{curl } \boldsymbol{A}$, to assure that $\boldsymbol{B}$ is solenoidal, then leads to

$$\nabla^2 A = 0 \tag{5}$$

where a Coulomb gauge has been adopted (i.e., div $A = 0$).

Equation (5) is a vector relationship, implying that radial and azimuthal components of A are cross coupled in cylindrical coordinates. The vector potential should be continuous across surfaces of discontinuity representing magnet locations on the hull ($r = R_i$ for $|z| \le Z_0$), shroud ($r = R_0$ for $|z| \le Z_0$), and struts ($\theta = n\pi/4$ for $Z_i \le |z| Z_0$, where $n = 0, 1, \ldots, 7$). Information on nomenclature is given in Fig. 13, which will be discussed further later. Symmetry allows restriction to one particular azimuthal segment, say $|\theta| \le \pi/8$. Jump conditions on magnetic field[14] can be expressed as

$$\begin{aligned} &\boldsymbol{e}_r \cdot [\boldsymbol{B}] = O, \quad \boldsymbol{e}_r \times [\boldsymbol{B}] = \mu \boldsymbol{K}^{(i)} \quad \text{on } r = R_i \\ &\boldsymbol{e}_r \cdot [\boldsymbol{B}] = O, \quad \boldsymbol{e}_r \times [\boldsymbol{B}] = \mu \boldsymbol{K}^{(0)} \quad \text{on } r = R_0 \\ &\boldsymbol{e}_\theta \cdot [\boldsymbol{B}] = O, \quad \boldsymbol{e}_\theta \times [\boldsymbol{B}] = \mu \boldsymbol{K}^{(s)} \quad \text{on } \theta = 0 \end{aligned} \tag{6}$$

where $\boldsymbol{K}$ denotes the surface current on the respective surfaces and $\boldsymbol{e}_z$, $\boldsymbol{e}_\theta$, and $\boldsymbol{e}_r$ are unit vectors in the coordinate directions. Brackets denote change in value from $R_i - 0$ to $R_i + 0$, etc. For calculations reported here, symmetry about $z = 0$ is assumed, B_θ increases 6 T across the hull at $z = 0$, and total current through a coil pair is conserved.

Other boundary conditions are as follows. Nonsingular behavior on $r = 0$ requires that $\partial A_z/\partial r = A_\theta = A_r = 0$. It is also fairly easy to establish that B_θ and B_r must be even functions of z and that B_z is odd in z. Similarly, B_z and B_r are odd functions of θ, B_θ is even, and the period in each case is $\theta/8$. This was established numerically to apply across struts as well, using a somewhat more general formulation than is described here. These observations imply symmetries for the vector potential. Finally, the magnetic field must vanish in the farfield as $z^2 + r^2 \to \infty$.

The boundary-value problem outlined earlier has been solved numerically. A three-dimensional finite difference treatment was used based on a second-order accurate formulation and an alternating direction implicit (ADI) solution procedure. Block 2×2 coupling was employed for A_θ and A_r in the azimuthal direction, but otherwise the scheme involves scalar forms and is quite analogous to implicit approximate factorization. A typical grid is shown in Fig. 14. It involves 36 grid points in the axial direction, 22 in the azimuthal direction, 35 in the radial direction, and nonuniform spacing to allow an

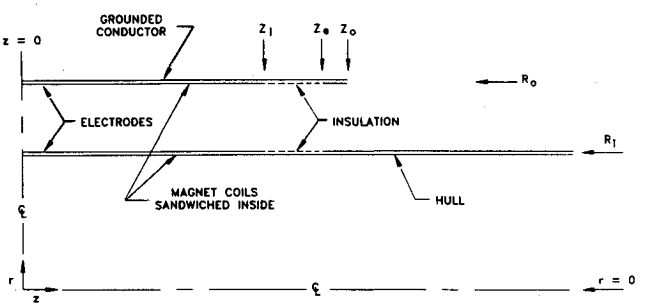

Fig. 13 Geometry and nomenclature for model problem.

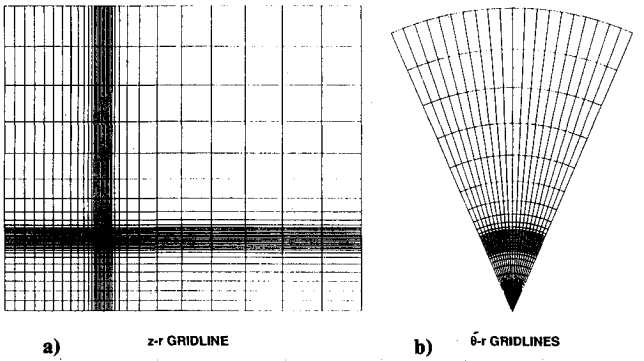

Fig. 14 Three-dimensional grid for numerical study.

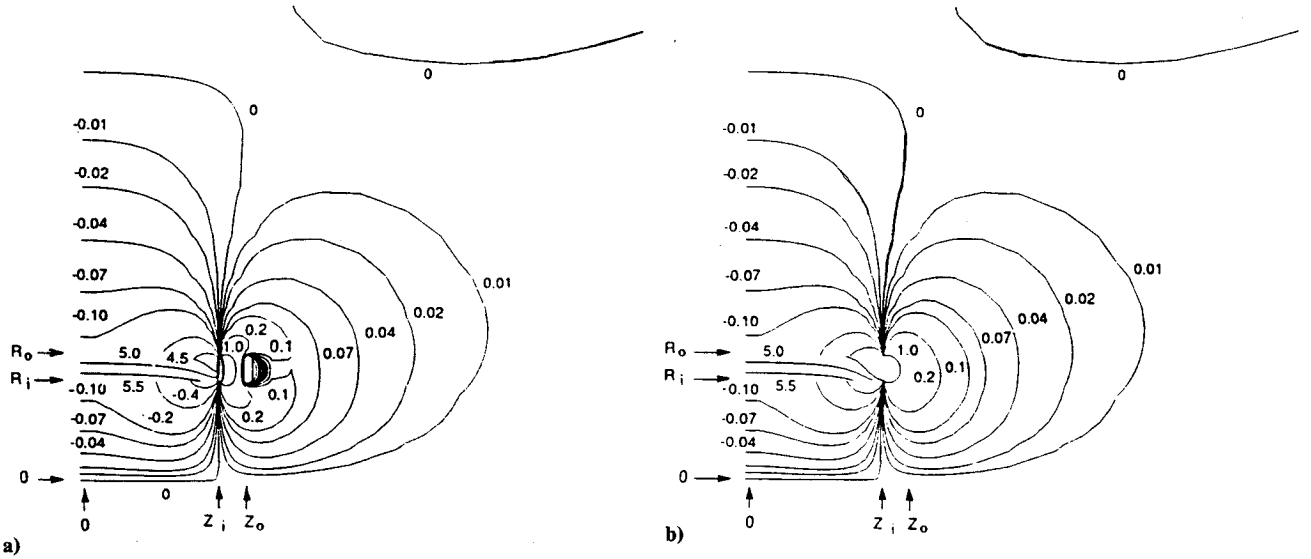

Fig. 15 B_θ **contours on two azimuthal planes: a) strut plane:** $\theta = 0$**; b) symmetry plane:** $\theta = \pi/8$.

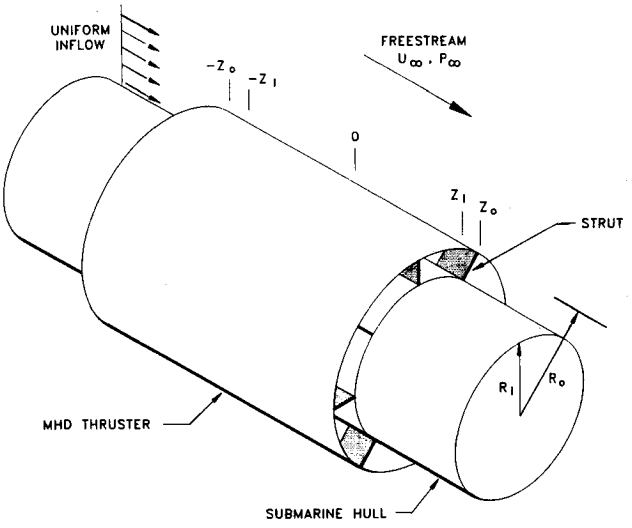

Fig. 16 Configuration for three-dimensional flowfield calculation.

economical computation with good resolution in high gradient regions. Also, the spacing varies smoothly to assure that second-order accuracy is maintained. Use of cyclic pseudotime step selection achieves rapid convergence, reducing residuals to 32-bit machine accuracy in 100–150 iterations for the grid in Fig. 14.

The result for B_θ is given in Fig. 15 on two azimuthal planes, as indicated. Only the region $z > 0$ is shown. Parameter values are $Z_i = 8.5$ m, $Z_0 = 10.0$ m, $R_i = 6.3$ m, and $R_0 = 7.8$ m. The magnetic field within the MHD channel is in the 4.5–6 T range for this case, and it undergoes rapid reduction in the end-turn region with considerable azimuthal dependence. On the other hand, farfield behavior for $r^2 + z^2 \to \infty$ is essentially independent of θ and is equivalent to a dipole distribution roughly centered on two circles; $r = (R_i + R_0)/2$ for $z = \pm Z_i$. Results in Fig. 15 should be viewed with care. The modeling does not account for magnetic permeability of the hull, so the field in $r < R_i$ is considerably overestimated. Also, no attempt has been made to minimize leakage into the external environment.

Next consider the electric field for the arrangement depicted in Fig. 13. This involves electrodes within the MHD channel ($|z| < Z_i$), an electrically insulated section (dashed line for $Z_i < |z| < Z_e$, and a grounded hull and shroud outside to suppress stray leakage. Insulated and grounded portions of the struts are similarly located axially. Struts and cylindrical shells are again treated as infinitesimally thin, but the superconducting coils are to be understood as sandwiched between the electrical features now addressed. Electric field stress concentrations arise due to the sharp shroud trailing edge and at junctures between conductor and insulator, but that is not viewed as critical for present purposes. Well-known design methods can be applied to relieve such effects.[15]

The first part of Eq. (4) guarantees the existence of an electric potential such that $\boldsymbol{E} = \text{grad}\ \phi$. Requiring $\boldsymbol{J}$ to be solenoidal for a medium with uniform conductivity then leads to

$$\nabla^2\phi = \mu \boldsymbol{U} \cdot \boldsymbol{J} - \boldsymbol{B} \cdot \text{curl}\ \boldsymbol{U} \tag{7}$$

For an efficient MHD propulsion system ($J < 500$ A/m^2), the first term on the right-hand side of Eq. (7) is small compared with the effect of applied voltage. To decouple flow and electric field calculations, it will also be assumed that $\boldsymbol{U}$ is constant. In that case, ϕ satisfies Laplace's equation. Note that the variation of the Lorentz force across boundary layers is now suppressed in consequence, something that should be reconsidered in later work.

There remains an effect of flow on the electric field through the requirement $\boldsymbol{n} \cdot \boldsymbol{J} = 0$ on all insulated surfaces. We have assumed $\boldsymbol{U} = U_\infty \boldsymbol{e}_z$ where U_∞ is the freestream axial flow speed. This is a reasonable approximation for inviscid flow since the δU across a realistic, well-designed MHD thruster is small. Boundary conditions on conducting surfaces are $\phi = -V$ on the (interior) shroud electrode and $\phi = 0$ everywhere else. This implies radially inward current flow and positive B_θ, as we have so far chosen coordinate directions, to produce forward thrust. In addition, ϕ should be an even function of z as well as θ, $\partial\phi/\partial r = 0$ on $r = 0$, and $\boldsymbol{E} \to 0$ for $r^2 + z^2 \to \infty$. The noted symmetry in θ is not obvious across a strut, but it was found to be true, albeit with strong discontinuities in $\partial\phi/\partial\theta$ across $\theta = 0$.

The boundary-value problem for ϕ has been solved numerically using an ADI procedure using the same grid as in Fig. 14. Specific results will not be given to conserve space. Suffice it to state that grounded exterior portions of the struts and shroud (for $Z_e < |z| < Z_0$) are effective in containing electric field within the propulsor. The more interesting quantity for present purposes is the Lorentz force, $\boldsymbol{F} = \boldsymbol{J} \times \boldsymbol{B}$, obtained from these calculations. Those results are given in the next section.

Inviscid Three-Dimensional Flow Results

One of the main reasons for undertaking the present study was the need to assess the effect of nonuniform Lorentz force

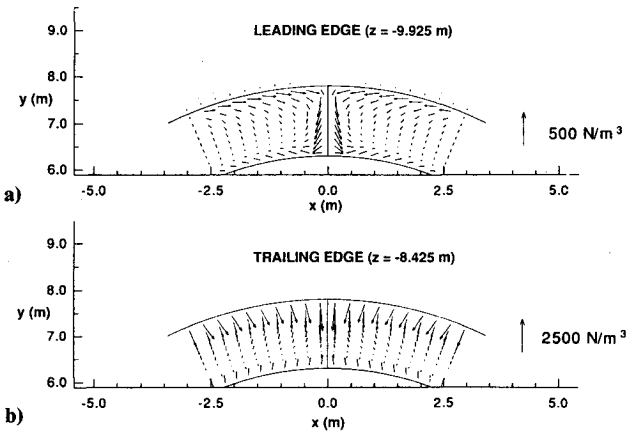

Fig. 17 Transverse Lorentz force at upstream strut leading and trailing edges.

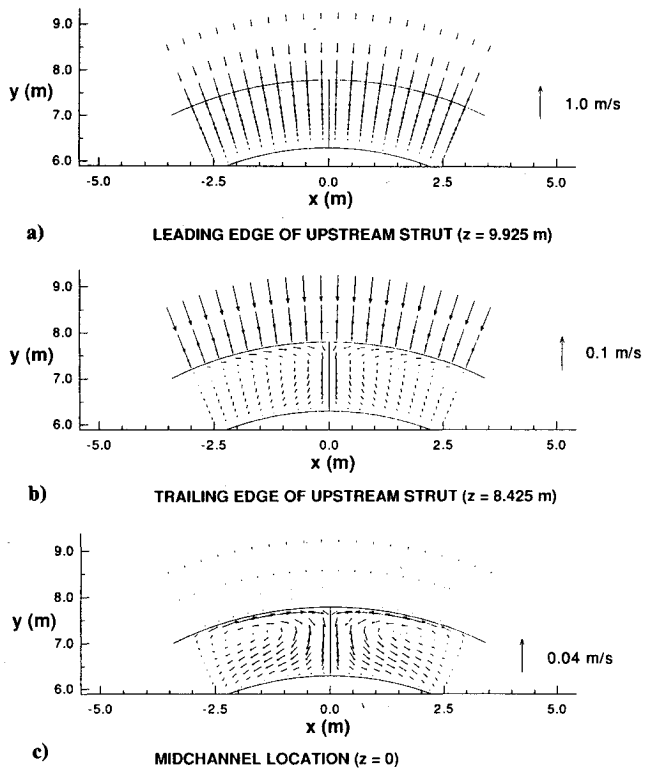

Fig. 18 Crossflow velocity evolution for uniform inflow.

on flow in the end-turn region. Preliminary results given here focus on the inlet region where the flow capture process is predominantly inviscid. In contrast to idealized electromagnetic results discussed earlier the flowfield is not at all symmetrical in z because there is a preferred direction. We have considered the full configuration in Fig. 16, using reflection rules for the Lorentz force. This involves a constant radius hull, upstream and downstream struts, and a total MHD thruster length of 20 m. Only the case of uniform inflow velocity profile will be treated. Consideration of vortical inflow would be of interest, but that is not easy to do numerically with a zero thickness strut and inviscid flow.

Results will be given at three crossflow planes: the upstream strut leading edge ($z = -Z_0$), its trailing edge ($z = -Z_i$), and at the midchannel location ($z = 0$). Vector plots of the transverse Lorentz force components are shown in Fig. 17 for only two of these locations because it vanishes at $z = 0$. Scales are adjusted based on local magnitude, as indicated, to provide a more meaningful visualization. Note that the transverse Lorentz force is about five times stronger at $z = -Z_i$ than it is at $z = -Z_0$. The F_r is seen to be symmetrical about $\theta = 0$ and F_θ is clearly antisymmetrical. Although not shown, there are regions of adverse axial body force near boundaries. These would affect a viscous flowfield more, particularly in conjunction with adverse pressure gradient as in Fig. 7 near the shroud trailing edge.

Corresponding results for the inviscid flowfield are shown in Fig. 18 for $z \leq 0$. The crossflow is radially inward at the upstream strut leading edge, as expected from two-dimensional results discussed earlier. The magnitude of v_r is small compared with $U_\infty = 10$ m/s. This is consistent with little streamtube contraction in the capture region and $\Delta v_z / U_\infty \sim 0.1$ typically through the MHD thruster. Notable secondary flow has developed by the strut trailing edge. The transverse Lorentz force continues to be significant for a channel height or so downstream, leading to further evolution of the secondary flow at the midchannel location. In all cases, the transverse velocity components are small. This is largely due to extending the magnets well outside the electrodes to allow current decay. Based on prior studies of horseshoe vortex formation,[16,17] it is fairly clear that secondary flow effects arising from vorticity in an incoming hull boundary layer will dominate body force effects.

Conclusions

This paper has focused on the development of detailed analysis tools for computation of hydrodynamic and electromagnetic aspects of marine MHD propulsion concepts. Idealizations have been employed, primarily to shift the focus toward top-level understanding of some of the basic issues. Certain aspects have also been avoided to render an introductory exposition more tractable. This includes two-phase flow associated with production of electrolysis bubbles at the MHD electrodes. Specific conclusions are as follows.

1) A scalar-implicit formulation, based on pseudocharacteristic relations for Chorin's modified equations, provides an efficient method for solving both inviscid and viscous incompressible flow problems. It can be applied to multiply connected domains and two-equation turbulence modeling with excellent code robustness.

2) Significant flow contraction occurs in the inflow capture region. Suitable contouring of the shroud in that region, perhaps with flaring, could be appropriate to prevent separation and related effects associated with the local pressure minimum.

3) Further assessment of proper design near the shroud trailing edge is also needed to alleviate the influence of adverse pressure gradient. Finite shroud thickness is necessary for a realistic superconducting magnet design.

4) Highly three-dimensional electromagnetic fields arise in the magnet end-turn regions. Those regions are also predominantly responsible for far-field magnetic behavior, which exhibits dipole character at large distances.

5) Secondary flow effects due to nonuniform Lorentz force in the end-turn region are small. This is largely due to extending the magnets well outside the electrodes to allow current decay. Vortical flow effects, not considered herein, are expected to dominate.

Acknowledgments

The work reported in this paper was supported by Avco Research Laboratory, Inc., Internal Research and Development funds. The authors would like to thank their management for permission to publish this material.

References

[1]Doragh, R. A., "Magnetohydrodynamic Ship Propulsion Using Superconducting Magnets," *Society of Naval Architects and Marine Engineers Transactions,* Vol. 71, Nov. 1963, pp. 370-386.

[2]Way, S., "MHD Submarine Propulsion," Westinghouse Research Lab., Research Memo 62-111-600-ML, Pittsburgh, PA, Aug. 1962.

[3]Knight, C. J., and Choi, D., "Development of a Viscous Cascade Code Based on Scalar Implicit Factorization," AIAA Paper 87-2150, June-July 1987; also *AIAA Journal*, Vol. 27, No. 5, 1989, pp. 581—594.

[4]Choi, D., and Knight, C. J., "Computations of 3D Viscous Flows in Rotating Turbomachinery Blades," AIAA Paper 89-0323, Jan. 1989.

[5]Choi, D., and Knight, C. J., "A Study on H and O-H Grid Generation and Associated Flow Codes for Gas Turbine 3D Navier-Stokes Analyses," AIAA Paper 91-2365, June 1991.

[6]Chorin, A. J., "A Numerical Method for Solving Incompressible Viscous Flow Problems," *Journal of Computational Physics*, Vol. 2, Aug. 1967, pp. 12-26.

[7]Choi, D., and Merkle, C. L., "Application of Time-Iterative Schemes to Incompressible Flow," *AIAA Journal*, Vol. 23, No. 10, 1985, pp. 1518-1524.

[8]Rizzi, A., and Eriksson, L., "Computation of Inviscid Incompressible Flow with Rotation," *Journal of Fluid Mechanics*, Vol. 153, April 1985, pp. 275-312.

[9]Rogers, S. E., Chang, J. L. C., and Kwak, D., "A Diagonal Algorithm for the Method of Pseudocompressibility," *Journal of Computational Physics*, Vol. 73, No. 2, 1987, pp. 364-379.

[10]Rogers, S. E., and Kwak, D., "Upwind Differencing Scheme for the Time-Accurate Incompressible Navier-Stokes Equations," *AIAA Journal*, Vol. 28, No. 2, 1990, pp. 253-262.

[11]Coakley, T. J., "Turbulence Modeling Methods for the Compressible Navier-Stokes Equations," AIAA Paper 83-1693, July 1983.

[12]Chang, P. S., and Gessner, F. B., "Experimental Investigation of Flow Around a Strut-Endwall Configuration," AIAA Paper 90-1541, June 1990.

[13]Jackson, H. A., "Submarine Parametrics," *Proceedings of the International Symposium on Naval Submarines*, London, Royal Inst. of Naval Architects, May 1983 (Paper 3).

[14]Stratton, J. A., *Electromagnetic Theory*, McGraw-Hill, New York, 1941, pp. 230-247.

[15]Cobine, J. D., *Gaseous Conductors*, Dover, New York, 1958, Chap. 7.

[16]Knight, C. J., "Inviscid 3D Computation for a Stanitz Elbow," AIAA Paper 85-1330, July 1985.

[17]Choi, D., and Knight, C. J., "Computation of 3D Viscous Cascade Flows," AIAA Paper 88-0363, Jan. 1988; also *AIAA Journal*, Vol. 26, No. 12, 1989, pp. 1477-1482.